Seasonal trends in the wintertime photochemical regime of the Uinta Basin, Utah, USA

Marc L. Mansfield, Seth N. Lyman

Department of Chemistry and Biochemistry, Utah State University Uintah Basin, Vernal, Utah 84078, USA

5   *Correspondence to*: Marc L. Mansfield (marc.mansfield@usu.edu)

Abstract: Several lines of evidence indicate that the photochemical regime, i.e., the degree to which ozone production is either VOC- or NO_x-limited, varies with season in the Northern Hemisphere. VOC-sensitivity seems to be more likely in winter and NO_x-sensitivity in summer. For most regions, the question is patently academic, since excessive ozone occurs only in summer. However, the Uinta Basin in Utah, USA exhibits ozone in excess of regulatory standards in both winter and

10   summer. We have performed extensive F0AM box modelling to better understand these trends. The models indicate that in late December the Basin's ozone system is VOC-sensitive, and either NO_x-insensitive or NO_x-saturated. Sensitivity to NO_x grows throughout the winter, and in early March, the system is about equally sensitive to VOC and NO_x. The main driver for this trend is the increase in available solar energy as indicated by the noontime solar zenith angle. A secondary driver is a decrease in precursor concentrations throughout the winter, which decrease because of, first, a dilution effect as

15   thermal inversions weaken, and second, an emission effect because certain emission sources are stronger at colder temperatures. On the other hand, temperature and absolute humidity are not important direct drivers of the trend.

20

1. Introduction

The Uinta Basin of Utah and the Upper Green River Basin of Wyoming are the only locations worldwide with documented high wintertime concentrations of ozone that consistently exceed 70 ppb. This unique atmospheric phenomenon results because both basins are prone to persistent wintertime thermal inversions which trap ozone precursors in a tight boundary layer. A high surface albedo resulting from snow cover is also required (Schnell et al. 2009). Both basins are rural but are home to an active oil and natural gas extraction industry, which accounts for a major share of wintertime atmospheric emissions (Lyman et al. 2013 & 2018, Edwards et al. 2014). Interestingly, many urban valleys and basins have inversions and snow cover, but if anything, they are NO_x-saturated and titrate out ozone in winter (Shah et al. 2020, Li et al. 2021). The preferred explanation for the phenomenon is that the precursor speciation unique to the oil and gas industry is well-suited for winter ozone production (Schnell et al. 2009, Edwards et al. 2014, Ahmadov et al. 2015, Matichuk et al. 2017, Mansfield and Hall 2018).

Knowledge of the photochemical regime, or the degree to which an ozone system is either NO_x- or VOC-sensitive, is important in efforts to control ozone concentrations. It is well known that the ozone production efficiency, i.e., the number of ozone molecules generated for each NO_x molecule consumed (defined operationally as the slope of the least-squares trend line of O_x vs. NO_z concentrations) indicates the relative photochemical regime, with larger values indicating a shift towards relatively higher NO_x-sensitivity and vice versa (Sillman 1995; Sillman et al., 1997; Sillman et al., 1998; Sillman, 1999; Rickard et al., 2002; Sillman and He 2002; Seinfeld and Pandis 2006; Chou et al., 2009). Another photochemical indicator with the advantage that it can be determined from satellite measurements is the ratio of the column densities of HCHO and NO_2. Larger values of the column $HCHO/NO_2$ ratio also indicate a shift towards NO_x-sensitivity (Martin et al., 2004; Duncan et al., 2010; Choi et al., 2012; Jin et al., 2017).

In many regions of North America, Europe, and East Asia, studies based on models or on measurements of photochemical indicators have observed seasonal trends in the photochemical regime. It is common to see ozone systems that are more NO_x-sensitive in summer and more VOC-sensitive in winter (Kleinman 1991; Jacob et al., 1995; Liang et al., 1998; Martin et al., 2004; Jin et al, 2017). In this paper, we report a similar trend in the Uinta Basin, Utah, USA. For most regions, the question of winter vs. summer ozone chemistry is purely academic, because ozone concentrations in exceedance of regulatory limits only occur in summer. However, in the Uinta Basin exceedances occur in winter and summer. Therefore, an understanding of the transition takes on added importance.

50

Below we report box model calculations to determine the drivers for this trend and to estimate sensitivities to NO_x and VOC throughout the winter. The models indicate that in early winter, the Basin is either VOC-sensitive or NO_x-saturated, while in late winter, NO_x and VOC sensitivities are about the same. We show that the main drivers for the trend are the change in solar zenith angle and a decrease in average precursor concentrations over the course of the winter. Other meteorological trends, specifically mean temperature and mean absolute humidity, are not important drivers. We also consider the factors driving the decrease in precursor concentrations. The data support a dilution effect as inversions become less intense during the advancing season. There is also evidence for an emission effect: Certain emission classes,

such as engine efficiency or equipment used more frequently in cold weather, are linked directly or indirectly to the temperature. This improved knowledge of the Basin's photochemical regime allows us to suggest possible ozone abatement strategies.

Edwards et al. (2014) have also published box-model results for the Uinta Basin in winter. An important difference between their model and ours is the VOC speciation employed. Our speciation profile is reported below.

2 Methodology

2.1 Photochemical Indicators in the Uinta Basin

The Uinta Basin is a structural and sedimentary basin in eastern Utah, Fig. 1, that produces oil and natural gas. Unless stated otherwise, the data and models discussed here are from the Horsepool monitoring station at latitude 40.1434° and longitude –109.4689°. Figure 2 displays the ozone production efficiency, calculated daily as the slope of the least-squares trend lines of O_x vs. NO_z, and then averaged. Figure 3 displays the mean ratio of column HCHO data to tropospheric column NO_2 data obtained from the Ozone Monitoring Instrument (OMI, NASA-OMI 2022). The threshold between VOC and NO_x sensitivity is near 1 or 2 for both indicators, but the precise threshold depends on local conditions, and it is best to interpret the indicators in light of modelling results, as we do below. Nevertheless, the data indicate a seasonal trend, with the system tending towards VOC sensitivity in early winter, and NO_x sensitivity in late winter.
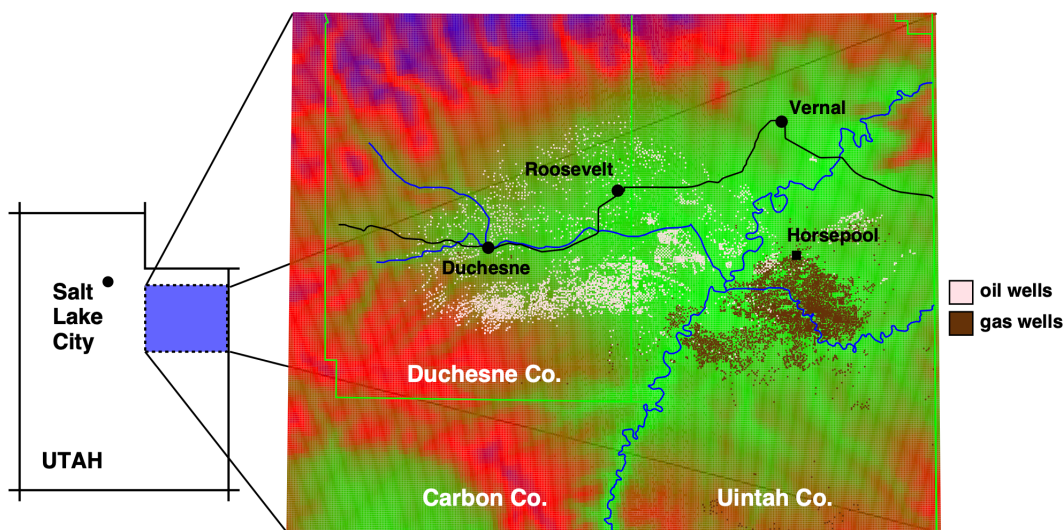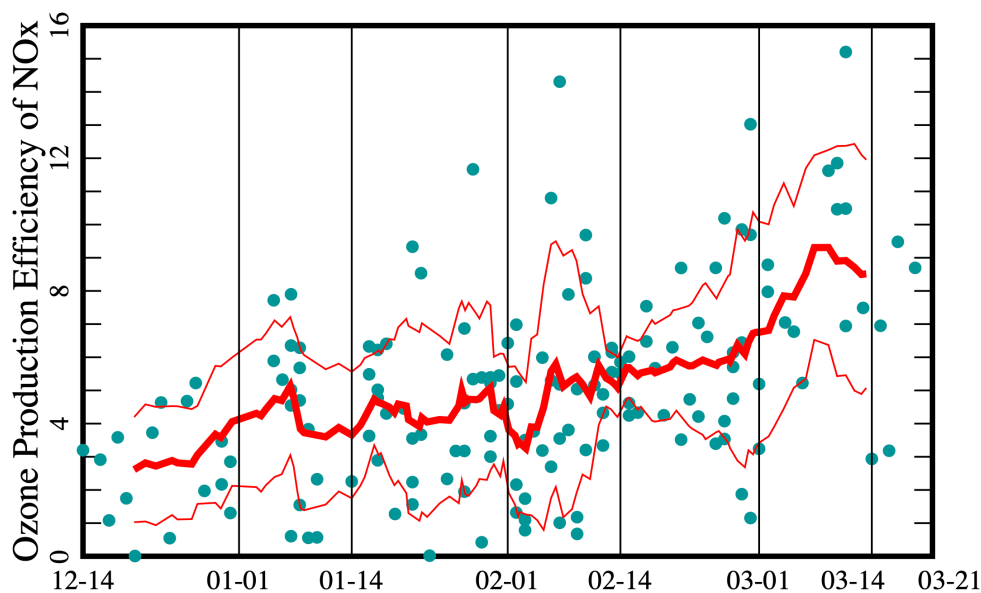

Figure 1. Map of the Uinta Basin. Duchesne, Roosevelt, and Vernal are major population centers. The Horsepool monitoring station and the distribution of oil and natural gas wells are also shown. Background coloration indicates surface elevation.

80

Figure 2. Ozone production efficiency at the Horsepool monitoring station in the Uinta Basin. Data from days when the hourly ozone concentration exceeded 60 ppb from 2011 to 2022 and from December to March are shown. The red traces show ten-point running averages plus or minus one standard deviation.
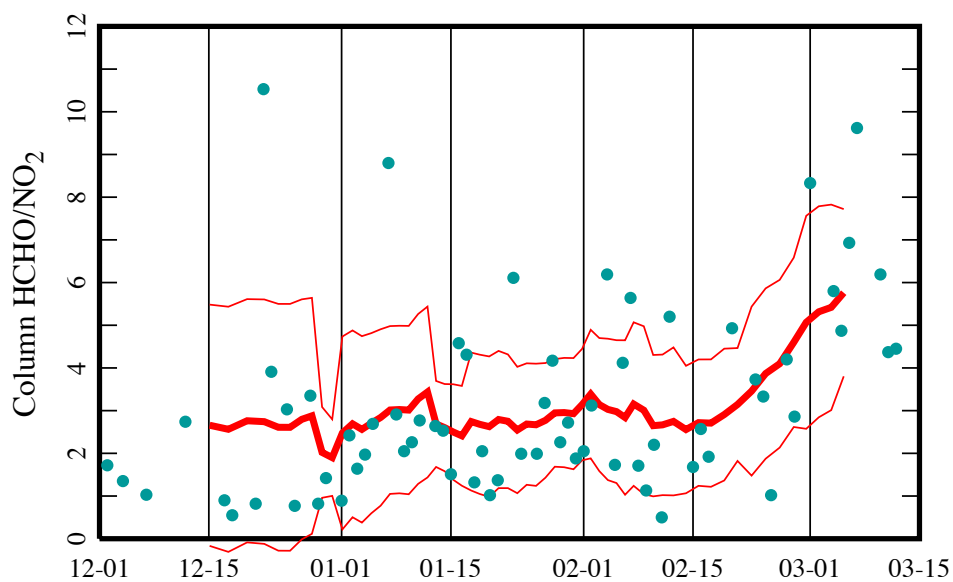
85

Figure 3. Mean ratio of column HCHO to tropospheric column NO₂ from the Ozone Monitoring Instrument (OMI) pixel that contains the Horsepool station, on the indicated date, including data from 2009 to 2020 and between 1 December and 15 March. The red traces show 10-point running averages, plus or minus one standard deviation.

2.2 Trends in meteorological variables and precursor concentrations

Any property that varies systematically through the season might conceivably be a driver for the trend in photochemical indicators seen in Figs. 2 and 3. This could include the actinic flux, the ambient absolute humidity, and the ambient temperature. Here, we take the noon-time solar zenith angle as a proxy for the actinic flux. This is permissible because during high ozone episodes, the sky is typically free of clouds and surface albedo contributed by snow cover is essentially uniform. The noon-time solar zenith angle is given to a good approximation by the formula

$$\theta = L + D\cos(\omega_E t) \qquad (1)$$

where L is the latitude (40.14° at the Horsepool station), D is the tilt of Earth's axis (23.44°), ω_E is the angular frequency of Earth's revolution ($2\pi\ y^{-1}$), and t is the time elapsed since the last winter solstice (Finlayson-Pitts and Pitts; 2000). Therefore, between the winter solstice and the vernal equinox, θ varies from about 63.6° to 40.1°. Figure 4 displays temperature and absolute humidity trends at the Horsepool station. Daily averages of temperature and absolute humidity between the hours of 11:00 to 20:00 MST, on dates from December 15 to March 15 and years between 2012 and 2021 are shown. (The rationale for computing means between the hours of 11:00 to 20:00 will be explained in Section 3, Calculation 4.) Throughout this work, the winter season has been divided into six fortnights or half-months, defined in Fig. 4. The fortnights will be designated "late December," "early January," and so on. Absolute humidity was calculated from measured values of temperature and relative humidity using a standard formula for the temperature dependence of the saturation vapor pressure of water (Seinfeld & Pandis; 2006).

NO$_x$ and methane concentrations are measured continuously at Horsepool during winter months, but non-methane organics are not. Therefore, we take methane as a marker for VOC concentrations, employing the conversion factor, explained below, of 0.0619 moles non-methane VOC for each mole of methane. Figure 5 indicates that NO$_x$ and methane concentrations are lower in late winter.

The available data indicate that a dilution effect caused by weakening inversions contributes to the systematic decrease in precursor concentrations. Tethersonde measurements do not occur on a regular basis in the Uinta Basin, so we rely on the correlation between surface temperature and altitude to obtain a quantitative measure of inversion strength (Mansfield and Hall, 2013; Mansfield and Hall, 2018). A similar approach has been adopted by other authors (Whiteman et al.; 2004; Largeron and Staquet; 2016). We define the daily "pseudo-lapse rate," Ψ, in terms of the slope of the least-squares trend line of the daily maximum surface temperature vs. altitude at a number of sites:

$$\Psi = -\frac{\partial T}{\partial z} \qquad (2)$$

To exclude points that often lie in the non-linear region of the temperature-altitude profile, we only include sites between 1400 masl (the floor of the Basin) and 2000 masl (Mansfield and Hall, 2013; Mansfield and Hall, 2018). The daily maximum temperature is used to focus on persistent, as opposed to diurnal inversions. Low values of Ψ indicate strong inversions with tight boundary layers, while high values indicate a well-mixed boundary layer. Figure 6 shows the variation in Ψ as the season progresses. Inversions are seen to be more intense in early winter. Figure 7 shows the correlation between precursor concentrations

and Ψ, and Fig. 8 shows the correlation between CH$_4$ and NO$_x$ concentrations. These correlations all confirm that precursors are more diluted late in the season because the mixing layer is deeper.
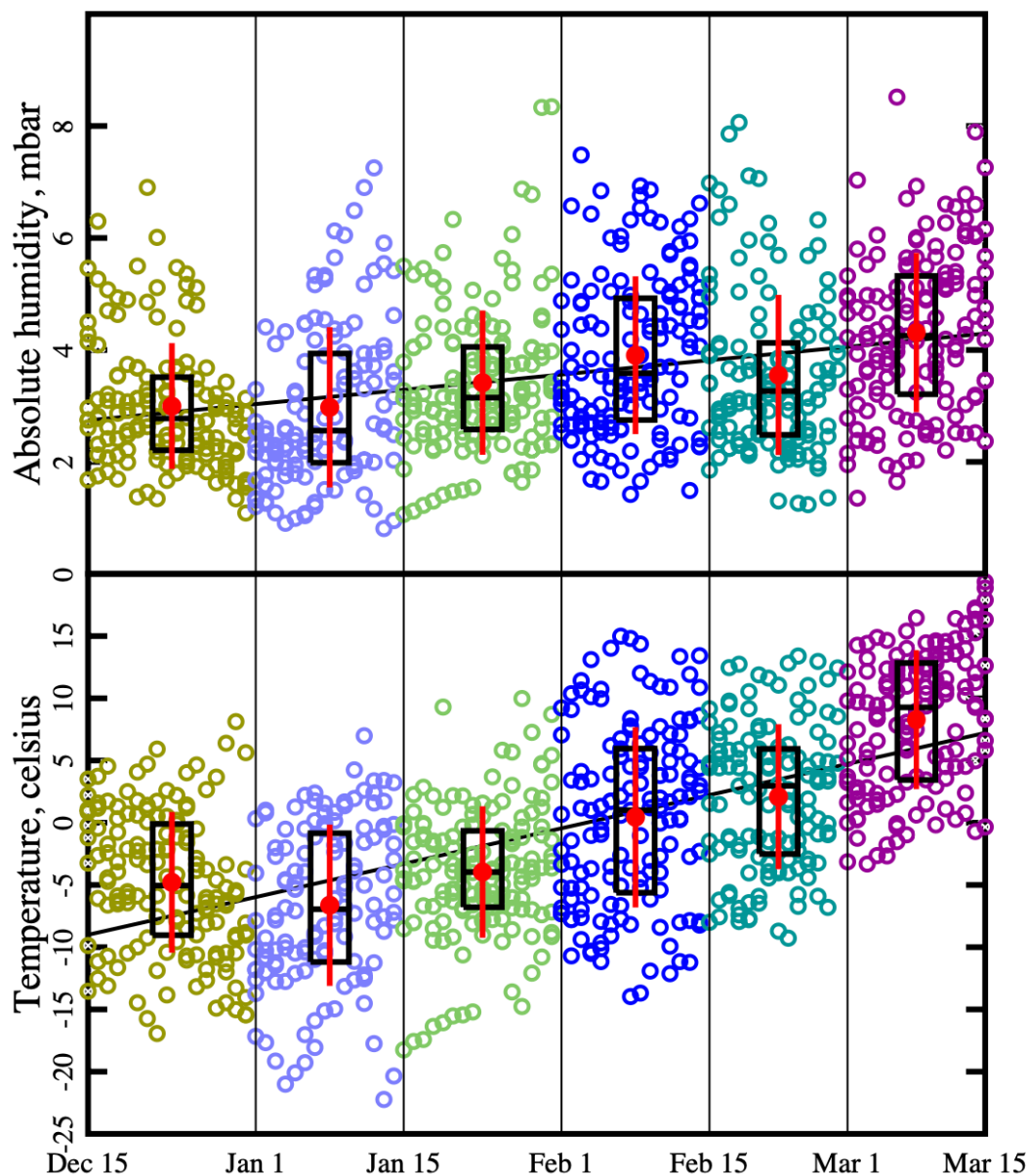
130

Figure 4. Absolute humidity and temperature trends throughout the winter. Humidity and temperature data are from the Horsepool monitoring station. Straight lines are the least-squares trend lines through the data points. Data are binned into six fortnights, late December, early January, etc. Black boxes show the 25th, 50th, and 75th percentiles. Red dots and whiskers show the mean plus or minus 135 one standard deviation.
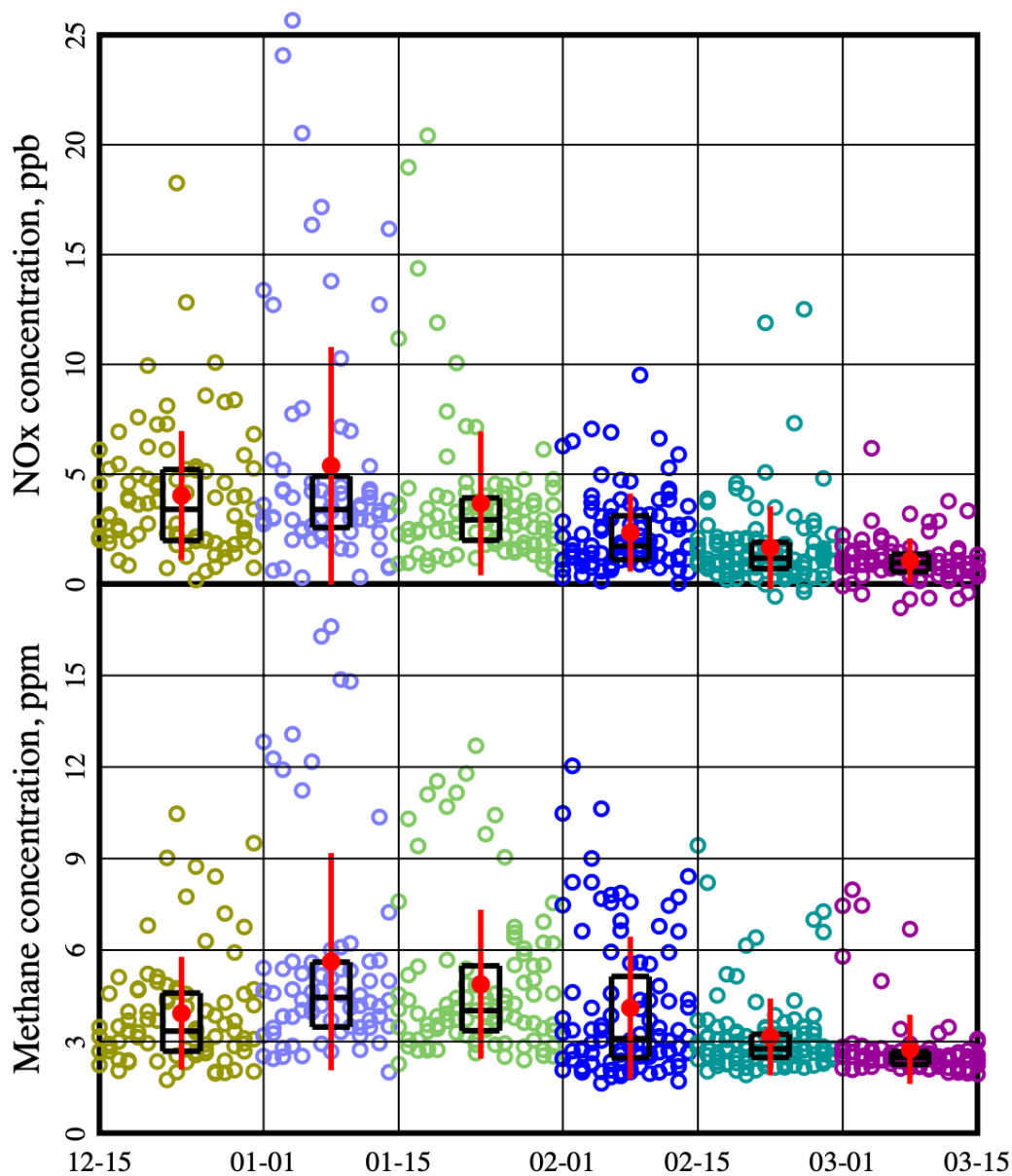
Figure 5. Average daily NOx and CH₄ concentrations measured at Horsepool. Each symbol is a daily average taken over the hours 11:00 to 20:00 MST. Only days when both NO_x and CH_4 data were reported have been displayed. Black boxes show the 25th, 50th, and 75th percentiles. Red dots and whiskers show the mean plus or minus one standard deviation.

140

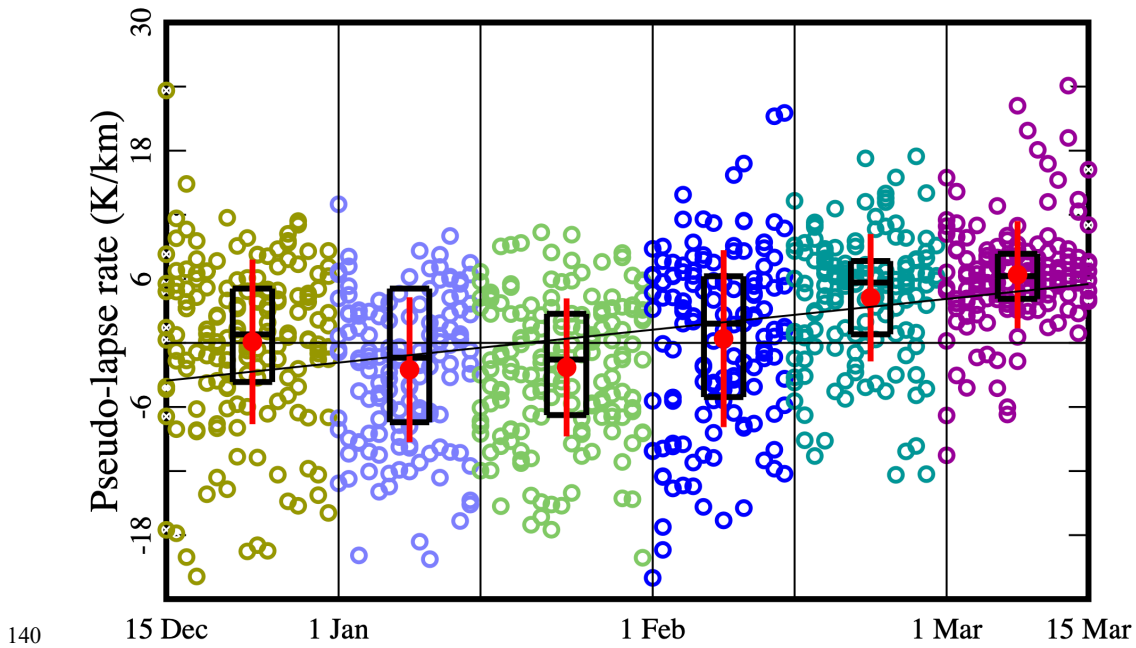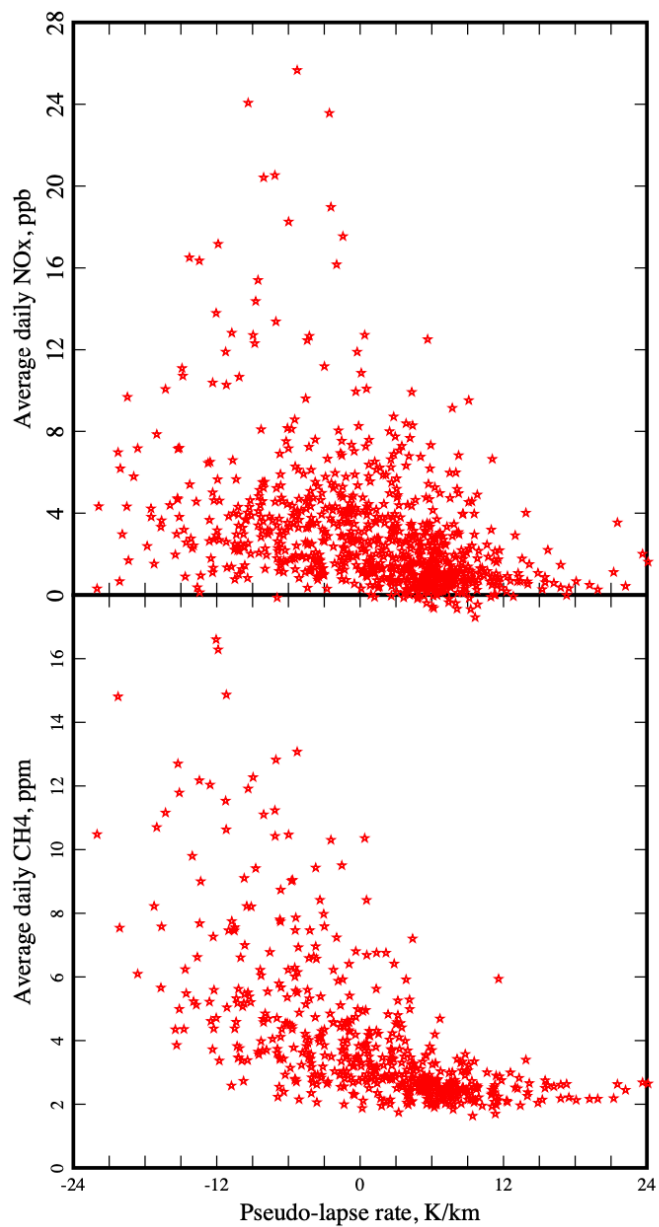**Figure 6. Variation in pseudo-lapse rate Ψ as the season progresses. Each symbol represents the calculation for one day. Black boxes indicate the 25th, 50th, and 75th percentiles. Red dots and whiskers display the mean plus or minus one standard deviation.**

Figure 7. Correlations between NO$_x$ and methane concentrations and the pseudo-lapse rate Ψ. Each symbol represents a daily average.
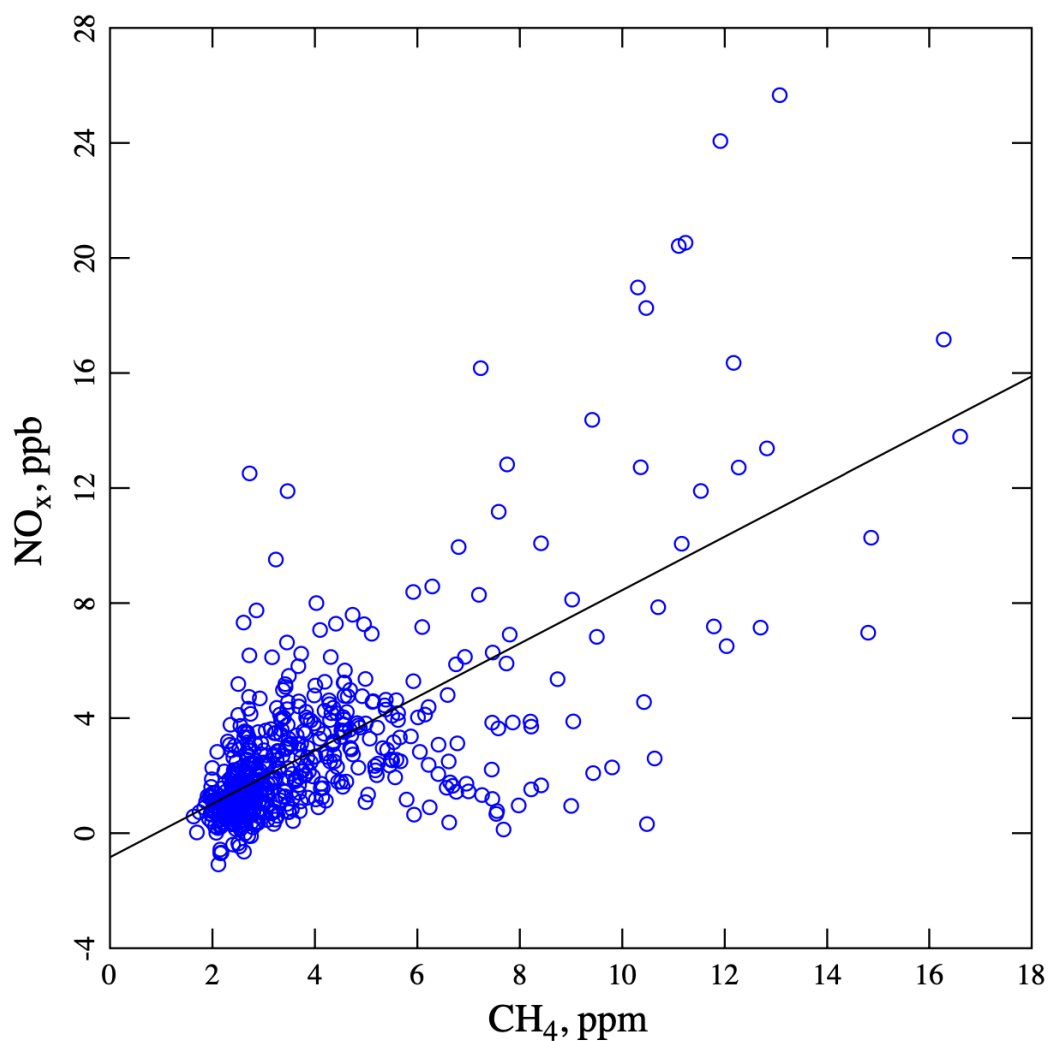
Figure 8. Correlations between NO$_x$ and methane concentrations. Each symbol represents a pair of daily averages.

150   However, emission effects might also contribute to the seasonal decline in precursor concentrations. Many studies find that
vehicular NO$_x$ emissions are greater in winter. Several causative factors are mentioned, including poorer engine performance in
the cold, cold starts, and operation of NO$_x$ after-treatment systems (e.g., catalytic converters) outside their optimal temperature
range (Dardiotis et al., 2013; Reiter and Kockelman, 2016; Saha et al., 2018; Suarez-Bertoa and Astorga, 2018; Grange et al., 2019;
Weber et al., 2019; Hall et al., 2020; Li et al., 2020; Wang et al., 2020; Bishop et al., 2022; Wærsted et al., 2022). Most studies
155   agree that the effect is present in light- and heavy-duty diesel vehicles (the predominant form of transportation near Horsepool),
while studies investigating the effect in gasoline vehicles give conflicting results, perhaps because of differences in NO$_x$ after-
treatment systems (Dardiotis et al.; 2013; Suarez-Bertoa and Astorga 2018; Grange et al., 2019; Li et al., 2020). Wærsted et al.
(2022) report vehicular NO$_x$ emissions to be about a factor of three larger at –12 °C than at +12°C in Norway. Hall et al. (2020)
report that vehicular NO$_x$ emissions in the Baltimore-Washington (USA) metropolitan area are about twice as large at –5 °C than

160   at 25 °C. Other studies give smaller ratios between summer and winter. Such variability likely results from variations in the composition of the local fleet (e.g., gasoline vs. diesel engines and older vs. newer NO_x after-treatment systems). The Uinta Basin is also home to other NO_x sources, such as well-site and portable natural gas-fueled heaters, that operate only in winter. We have been unable to find data on temperature trends in the NO_x emissions from drilling rigs, but these may behave similarly to diesel-powered vehicles. Hence, it is likely that dilution and emission effects both contribute to the decrease in NO_x concentrations. This

165   seasonal trend in NO_x concentrations obviously deserves more study.

Figure 5 indicates that methane concentrations also vary systematically as the season progresses. Any dilution effects, cited above, will similarly affect methane concentrations. But emissions correlated with ambient temperature may also contribute, for example, from equipment such as glycol dehydrators, heat trace pumps, and "hot oil" trucks, and from operations to thaw frozen lines,

170   including pipeline venting and well blowdowns. Like NO_x, this methane trend also deserves further study.

Note that methane concentrations are rarely below 2 ppm, i.e., in late winter, they approach but never fall below the global background concentration (NOAA 2022). This is additional evidence of a well-mixed boundary layer under certain conditions. Also note that the ratio of the largest to the smallest mean in Fig. 4 is about 2 for methane and about 5 for NO_x. However, we

175   should not read too much into that difference. More relevant is the level of CH_4 relative to background.

2.3 Box modelling procedures

We used the "Framework for 0-D Atmospheric Modeling" (F0AM) platform, version 4.2.1, in a configuration similar to Lyman, et al. (2022), which has been coded as MATLAB script (Wolfe et al.; 2016). A subset of the "Master Chemical Mechanism,"

180   MCM v3.3.1, served as the chemistry mechanism (Jenkin et al., 2003; Saunders et al., 2003; Jenkin et al., 2015; Zong et al., 2018; MCM, 2022). Descriptions of all other input variables are summarized in Tables 1 and 2. Representative MATLAB code and input files are included as Supplementary Material. Each simulation spanned four days, including three days of spin-up. According to Table 2, one VOC unit is equivalent to 4920 ppb of methane and 304.4 ppb of the non-methane hydrocarbons, alcohols, and carbonyl compounds listed there.

185   Table 1. Inputs to the box models.

Variable	Comments	Assigned value
VOC concentrations	Speciation profile from Table 2. One "unit" of input VOC implies the 59 compounds at the indicated concentrations. In any run, the total VOC concentration was set by scaling the total number of VOC "units." Species concentrations were held constant throughout the run (LinkSteps = 1, HoldMe = 1), equivalent to assuming VOC concentrations are at steady state with emission, deposition, and chemical transformation in balance.	One VOC unit = 4920 ppb CH_4 + 304.4 ppb of non-methane organics.
NO_x concentrations	"Family conservation" option switched on; NO_x = NO + NO_2 concentrations held constant throughout each hour. Hourly NO and NO_2 profiles prepared in several ways: (1) Observational data from a single day. (2) Averages of observational data from a number of	

	days. (3) Rescaling any of the profiles prepared by the previous two ways.	
Background ozone	Lyman et al., 2013; Lyman et al. 2018.	50 ppb
Temperature	Hourly data from a given day.	
Relative humidity	Hourly data from a given day.	
Barometric pressure	Hourly data from a given day.	Average over all models: 845 ± 7 (1σ) mbar.
CO concentration	Hourly concentration measurements from Horsepool on 2019-02-27.[a] CO concentration held constant throughout each hour (LinkSteps = 1, HoldMe = 1).	272 ppb (average from 11:00 to 20:00 MST)
k_{dil}, dilution factor	Same as Edwards et al., 2014.	$1.8 \times 10^{-5}\ hz$; daylight; $2.0 \times 10^{-6}\ hz$; dark
Solar zenith angle	Computed with the F0AM procedure sun_position from the time, date, latitude, longitude, and elevation at Horsepool.	
Albedo	Typical of snow surfaces at Horsepool.	0.7
Ozone column	From Giovanni NASA website (NASA, 2022).	275 DU
J_{corr}	Correction factor for scaling J-values (Wolfe et al., 2016).	0.5

[a]Due to an oversight, CO concentration data from 2019-02-27 were applied in all modeling runs. However, we verified that modeled ozone concentrations changed by no more than about 1 ppb even when we completely zeroed out the CO concentration.

190

Table 2. VOC concentrations in the F0AM box model (Lyman et al.; 2021). The concentrations listed here constitute one "unit" of VOC in the models.

Methane		Total	Aromatics		Total
methane	4920.0 ppb	4920.0 ppb	benzene	1.2 ppb	3.0 ppb
Non-methane Alkanes		Total	toluene	1.2	
ethane	123.0 ppb	264.8 ppb	o-xylene	0.1	
propane	63.0		m-xylene	0.2	
n-butane	25.0		p-xylene	0.1	
Isobutane	15.0		ethylbenzene	0.1	
n-pentane	10.0		1,2,3-trimethylbenzene	0.1	
Isopentane	11.0		n-propyl benzene	0	
n-hexane	4.0		isopropyl benzene	0	
2-methylpentane	3.0		1,2,4-trimethylbenzene	0	

12

3-methylpentane	2.0		1,3,5-trimethylbenzene	0	
2,2-dimethylbutane	0.3		1-ethyl-2-methylbenzene	0	
2,3-dimethylbutane	1.6		1-ethyl-3-methylbenzene	0	
n-heptane	1.9		1-ethyl-4-methylbenzene	0	
2-methylhexane	0.8		styrene	0	
3-methylhexane	1.2		Alcohols		Total
n-octane	0.8		methanol	10.0 ppb	12.6 ppb
n-nonane	0.2		ethanol	0.3	
n-decane	0.2		isopropanol	2.3	
cyclohexane	1.8		Carbonyls		Total
Alkenes and Alkynes		Total	formaldehyde	6.5 ppb	21.0 ppb
ethylene	1.1 ppb	3.0 ppb	acetaldehyde	2.9	
propylene	0.1		butyraldehyde	1.3	
acetylene	1.8		acrolein	1.6	
1-butene	0		methacrolein	0.6	
cis-2-butene	0		benzaldehyde	4.4	
trans-2-butene	0		acetone	3.0	
1-pentene	0		methyl ethyl ketone	0.7	
cis-2-pentene	0		propionaldehyde	0	
trans-2-pentene	0		valeraldehyde	0	
1-hexene	0		crotonaldehyde	0	
			cyclohexanone	0	

195

Often, we wanted to compare two models with the same absolute humidity profile but at different temperatures. To change the temperature without changing the absolute humidity of course requires an adjustment of the relative humidity.

200

Typically, ozone concentrations in the Basin grow for several days during a multi-day inversion episode, peaking near the end of the episode. [Lyman et al. 2013 & 2018] The models described below examined peak-ozone days.

205 **2.4 Definition of sensitivity**

Let x represent some independent variable in the model, for example, the concentration of a precursor, and let y represent a dependent variable, which for our purposes is almost always the maximum ozone concentration on day four of a simulation run. A small variation in the independent variable, dx, induces a change, dy, in the dependent variable. The fractional changes in the two variables are dx/x and dy/y. We define the sensitivity, S, of the dependent variable on the independent variable as the ratio of

210 these two fractional changes:

$$S = \left(\frac{dy}{y}\right)/\left(\frac{dx}{x}\right) = \frac{x}{y}\frac{dy}{dx} = \frac{d\ln y}{d\ln x} \tag{3}$$

A small, 1% say, change in x produces an $S\%$ change in y. By this definition S is unitless and is the slope of the tangent on a log-
215 log plot. When the independent variable is the NO_x or VOC concentration, we will use the notation S_{NO_x} and S_{VOC}, respectively.
S values were calculated by numerical differentiation using three separate runs at x and $x \pm dx$ for dx on the order of a few percent.
We use the phrases "NOx-saturated" to indicate $S_{VOC} > 0 > S_{NO_x}$, "VOC-sensitive" to indicate $S_{VOC} > S_{NO_x} > 0$, and "NOx-sensitive"
to indicate $S_{NO_x} > S_{VOC} > 0$.

3 Results

220 We performed five separate calculations to probe the effect of the systematic variations documented in Section 2.2.

3.1 Calculation 1. NO_x and VOC sensitivity of 24 different models.

We identified 24 peak-ozone days between 15 December and 15 March and between 2013 and 2021. Maximum one-hour ozone
concentrations on these days varied anywhere from 59 to 154 ppb. Observational values of meteorological data and of NO_x
concentrations were employed as input data. Input VOC concentrations were in the proportion given in Table 2. For each model,
225 we defined a "base case" using the observed NO_x concentrations and by scaling the input VOC concentration until the maximum
day-4 ozone concentration agreed with measurements. These 24 models are summarized in Table 3. Figure 9 shows how the VOC
and NO_x sensitivities of each of the base-case models vary throughout the season. In December and January, VOC sensitivities
are always larger than NO_x sensitivities, and NO_x sensitivities are often negative. In late winter, NO_x and VOC sensitivities are
typically comparable. The three late-winter base-case models (2019-02-27, 2013-03-03, 2019-03-06) have nearly equal
230 sensitivities to NO_x and VOC.

Table 3. List of F0AM models constructed.

Model	Date	Base-case concentrations		Mean temperature, Celsius	Mean absolute humidity, mbar
		VOC (multiples of Table 1)	NO_x, ppb (average between 11:00 and 20:00 MST)		
D13a	2013-12-16	2.25	7.04	−12.53	1.75
D20a	2020-12-21	0.30	4.91	−6.50	3.19
D13b	2013-12-30	1.6	6.24	−10.45	2.21
J21a	2021-01-05	0.5	3.41	−5.34	2.99
J15a	2015-01-07	0.9	13.07	+1.76	5.17
J20a	2020-01-08	0.45	3.32	−8.28	2.78
J13a	2013-01-10	1.7	12.05	−13.15	1.77
J16a	2016-01-17	0.65	2.83	+0.88	4.05
J21b	2021-01-17	0.5	2.81	−4.64	3.01

J13b	2013-01-26	2.5	4.62	−3.31	4.06
J14a	2014-01-27	0.75	2.47	−1.48	3.72
J16b	2016-01-29	0.65	3.51	−4.48	3.31
F19a	2019-02-01	0.60	2.74	−6.84	2.52
F13a	2013-02-06	1.3	4.65	−3.50	3.53
F17a	2017-02-06	4.00	0.76	+1.71	5.05
F20a	2020-02-06	0.25	2.73	−6.56	2.48
F14a	2014-02-08	0.5	4.56	+2.77	4.69
F16a	2016-02-12	1.00	3.18	+0.21	4.44
F19b	2019-02-14	0.55	2.87	−2.72	4.53
F13b	2013-02-17	2.4	1.81	−6.21	2.95
F13c	2013-02-21	1.05	3.14	−2.74	3.68
F19c	2019-02-27	0.85	1.35	−3.24	3.63
M13a	2013-03-03	1.55	2.29	+1.30	4.98
M19a	2019-03-06	0.15	1.12	−1.52	5.13

235   The late-winter convergence of S_{VOC} and S_{NOx} appears to result more from an increase in S_{NOx} than from a decrease in S_{VOC}. The trend line for S_{VOC} has a slope of −1.6 σ, for σ the standard deviation of the slope, and a p-value of 0.13 from a Mann-Kendall trend test (Mann, 1945; Kendall, 1975). Therefore, the downward trend in S_{VOC} may be real, but our results lack sufficient statistical power to confirm this. On the other hand, with a slope of +3.9 σ and a very small Mann-Kendall p, the upward trend in S_{NOx} is statistically significant.
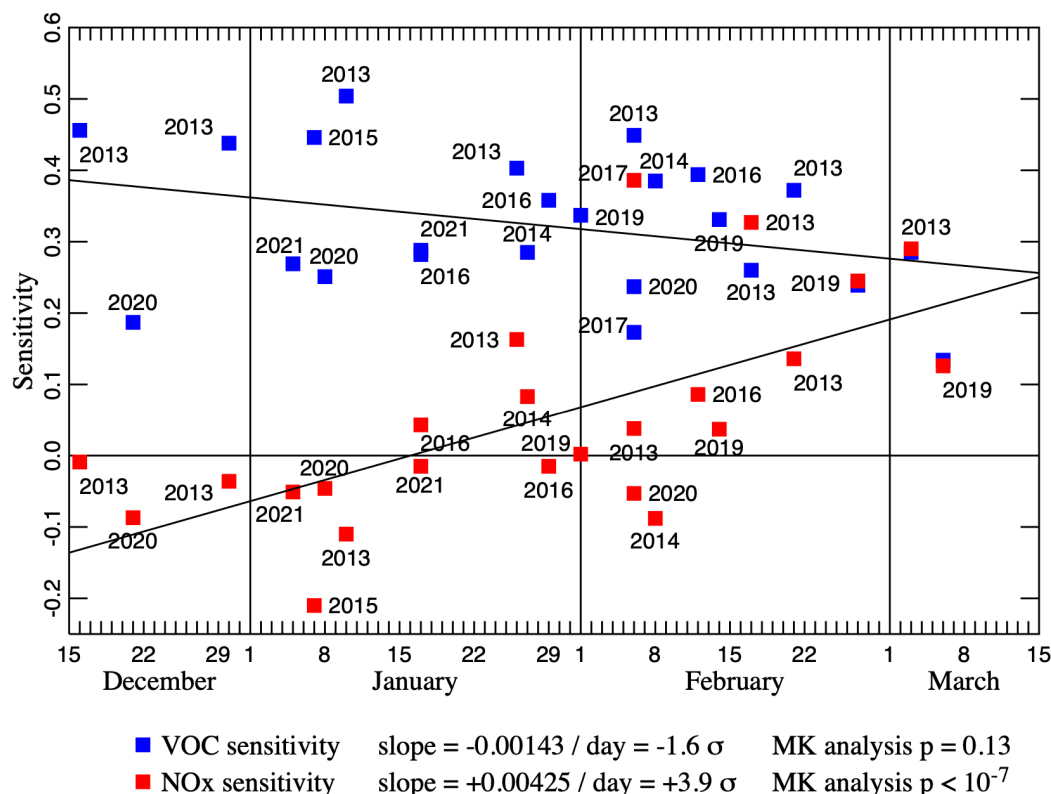
240

Figure 9. S_{VOC} and S_{NOx} **for 24 different box model runs. Slopes of the least-squares trend lines are given both as numerical values and as multiples of the standard deviations of the slopes. The *p*-values from Mann-Kendall trend analyses are also shown.**

245

3.2 Calculation 2. Impact of changing meteorological and concentration variables.

We examined five variables as candidate drivers for the change in photochemical regime documented above, namely, VOC concentration, NO_x concentration, solar zenith angle (SZA), ambient temperature (T), and ambient absolute humidity (AH). Starting from one of the models in Table 3, we replaced just one of the above five variables with typical values from either an

250   earlier or a later model. No other input quantity was varied. The solar zenith angle was varied by changing the date of the simulation. This lets us probe the effect of just one variable on S_{NOx} and S_{VOC}. Figure 10 plots the change in sensitivity, ΔS_{NOx} or ΔS_{VOC}, induced by the change in one of the five variables, solar zenith angle (Δ SZA), NO_x concentration (Δ NO_x), VOC concentration (Δ VOC), temperature (Δ T), and absolute humidity (Δ AH). For ease of interpretation, whenever one of the five variables trends downward during the winter (Equation 1 and Figs. 4 and 5) the scale of the corresponding abscissa in Fig. 10 is

255   shown in descending order. In this way, we see immediately whether modulating the variable tends to increase or decrease the sensitivity over the course of the winter. The scale of the ordinates in either row is identical, so the vertical displacement of each trend line indicates the relative strength of each individual driver. Most notably, the response to AH is very weak, indicating that absolute humidity is not an important driver. Traditionally, either the condition $|slope|/\sigma > 2$ or $p_{MK} < 0.05$ indicates a statistically significant trend in a dataset. Therefore, of the eight remaining trends depicted in Fig. 10, the ΔS_{VOC} vs. Δ NO_x is least likely to

260   be statistically significant. Normally, we expect each trend line to pass near the origin: A small change in only one variable usually

16

leaves the model largely unchanged. The two trend lines relative to Δ NO$_x$ fail to pass near the origin because the NO$_x$ variable is defined as an average over a daily profile. Therefore, Δ NO$_x$ = 0 can occur even if the models are not equivalent. This also explains the greater scatter in the two Δ NO$_x$ plots.
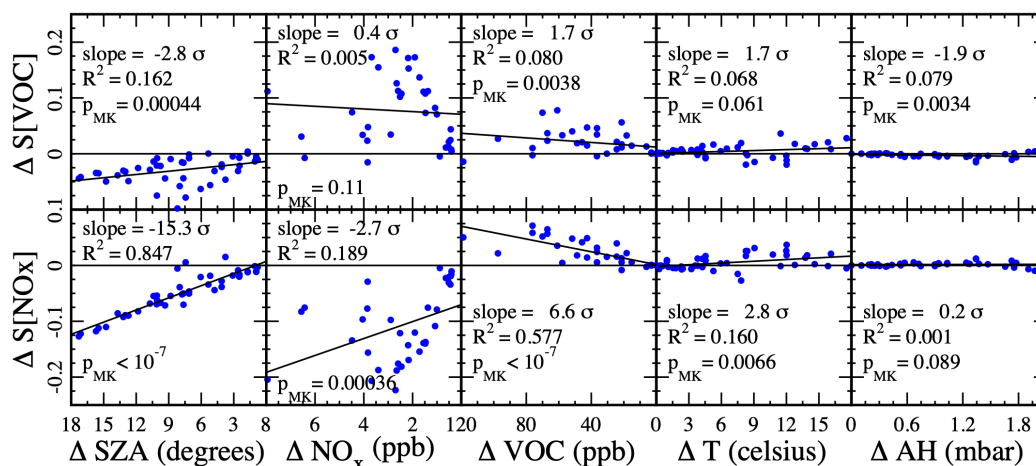
Figure 10. The change in sensitivity, ΔS_{NOx} or ΔS_{VOC}, induced by the change in one of the five variables, solar zenith angle (Δ SZA), NO$_x$ concentration (Δ NOx), VOC concentration (Δ VOC), temperature (Δ T), and absolute humidity (Δ AH) for various models listed in Table 3. The scale on the abscissa appears in descending order if the corresponding variable trends downward during the winter. The slope of each trend line as a multiple of its standard deviation, the value of Pearson's R^2, and the Mann-Kendall p-value are shown for each data set.

The total vertical displacement of each of the trend lines in Fig. 10 is one measure of the contribution of each of the five drivers to the seasonal sensitivity trends. Trend lines in the temperature and absolute humidity plots are relatively flat, indicating that the solar zenith angle and the NO$_x$ and VOC concentrations are the important drivers. Table 4 displays the values of all vertical displacements. Uncertainties were calculated from the standard deviations of the slopes. Sums of all five displacements are also tabulated. The uncertainty in the sums was calculated by propagating the uncertainties in each addend into the sum. The ΔS_{VOC} total is statistically zero, consistent with the finding that the S_{VOC} trend in Figure 9 may not be statistically significant. The solar zenith angle and the NOx concentration make comparable positive contributions to S_{NOx}, while the VOC concentration makes a smaller negative contribution.

Table 4. Vertical displacement of trend lines in Figure 10.

Variable	ΔS_{VOC}	ΔS_{NOx}
SZA	0.035 ± 0.012	0.131 ± 0.009
NOx	-0.019 ± 0.046	0.121 ± 0.044
VOC	-0.025 ± 0.015	-0.068 ± 0.010
T	0.010 ± 0.006	0.019 ± 0.007
AH	-0.004 ± 0.002	0.0005 ± 0.0022
TOTAL	-0.003 ± 0.050	0.20 ± 0.05

3.3 Calculation 3. Ozone isopleth diagrams.

285   We calculated an ozone isopleth diagram for each of the 24 models in Table 3 by scaling NO_x and VOC concentrations relative to the base model. Each F0AM run required approximately 2 to 4 minutes on a MacBook Pro laptop and generating the full diagram at high resolution proved to be too time-consuming. Rather, we calculated pixels at high resolution only around the boundary of the diagram, and at lower resolution throughout the interior. Pixels were also calculated at higher resolution in the vicinity of the "indicator curves," to be defined below. The ozone isopleth surface at all remaining pixels was generating by kriging interpolation

290   (Kerry and Hawick, 1998). All 24 diagrams are given in the Supplementary Material.

3.4 Calculation 4. Superposition of individual models to create ozone isopleth diagrams for each fortnight.

According to Calculation 2, the only relevant variables are solar zenith angle and the precursor concentrations. This implies that all isopleth surfaces belonging to any one fortnight are approximately superposable. The VOC concentration unit, defined in reference to Table 2, is directly transferable between different models, but the NO_x concentration unit, defined in reference to the

295   daily NO_x profile, is not. To test superposability, we assigned a different scale factor to the NO_x axis of each diagram and adjusted its value to optimize the superposition among all models from a given fortnight. We found that the scale factor for each model correlated best with the average NO_x concentration taken over the hours 11:00 to 20:00 MST and adopted this average to redefine the NO_x concentration axis on the ozone isopleth surfaces. For consistency, we have also used averages over the same hours, 11:00 to 20:00 MST, to report values of other variables.

300

Ozone isopleth surfaces for each of the 24 models listed in Table 3 were then superposed into six composite surfaces, one for each fortnight, and are shown in Fig. 11. All contributions defined at a given pixel on the original surfaces were averaged to estimate the ozone concentration in the composite pixel. Discontinuities in the contour curves occur because the diagrams of the individual models were not constructed with the same boundaries and because the individual models are not perfectly superposable.

305   Nevertheless, the discontinuities are generally not large, validating the superposability assumption. The domains defined by the 25th and 75th percentiles in Figs. 4 and 5 appear in Fig. 11 as white rectangles, and therefore define the domains at which precursor concentrations are at their typical values. The small white squares indicate points at which $S_{NOx} = 0$. The small pink squares indicate points at which $S_{NOx} = S_{VOC}$. These small squares define indicator curves: All points below the pink trace satisfy $S_{NOx} > S_{VOC}$ and constitute the region of NO_x sensitivity. All points above the white trace satisfy $S_{NOx} < 0$ and constitute the NO_x-saturation

310   region. All points between the two traces satisfy $S_{VOC} > S_{NOx} > 0$ and constitute the VOC-sensitive region. The indicator curves from each individual model are shown. The fact that these are all approximately superposable is further vindication of the superposability assumption.
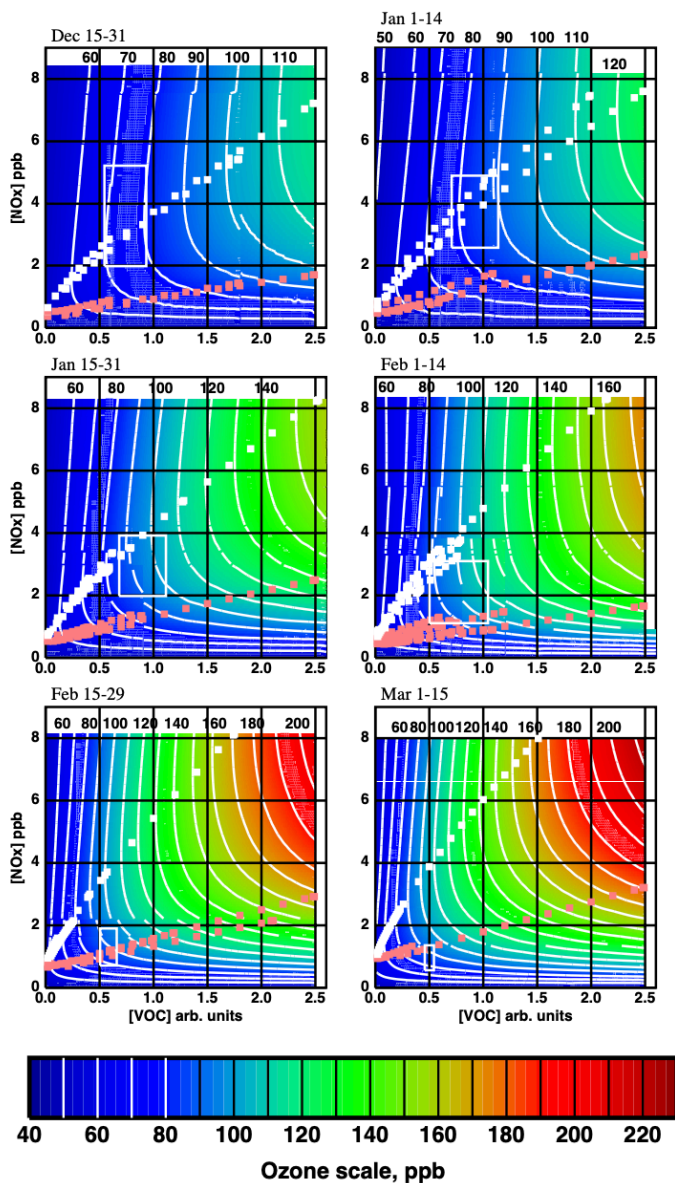
Figure 11. Composite ozone isopleth surfaces constructed from the 24 models listed in Table 3. White squares define the locus of points at which $S_{NOx} = 0$. Pink squares define the locus of points at which $S_{NOx} = S_{VOC}$. White rectangles were derived from the 25th-to-75th percentile boxes in Figs. 4 and 5 and therefore display the typical ranges of VOC and NO$_x$ concentrations.

3.5 Calculation 5. Impact of meteorology on ozone concentrations

It is obvious in Fig. 11 that at any given value of VOC and NO$_x$ concentrations, ozone concentration increases as the season progresses. Although our primary focus is seasonal trends in the photochemical regime, we have also performed box model calculations to analyze the trend in the ozone concentration itself. We have calculated temperature, absolute humidity and noon-time solar zenith angle sensitivities, S_T, S_{AH}, S_θ, for the 24 models, obtaining the approximate ranges given in column 2 of Table 5. The third column summarizes the change in the variable over the course of the season and was extracted from Equation 1 and

325 Fig. 4. Column 4 gives the percentage change in the variable through the season. Multiplying columns 2 and 4 yields column 5, an estimate of the percentage change in ozone concentration induced by the change in each variable. All three variables exert a positive influence on ozone concentration. The predicted total change in ozone concentration is in the range of 40% to 65% from December to March. Contributions from temperature and absolute humidity are much weaker than that from the solar zenith angle. We conclude that most of the increase in ozone concentration observed over the course of the winter at constant NO_x and VOC
330 concentration is driven by the change in actinic flux.

Table 5. Sensitivities of ozone concentrations to noon-time solar zenith angle (θ), temperature (T), and absolute humidity (AH).

$x =$	Range of S_x (25th to 75th percentile)	Range of x	% change in x from December to March	% change in $[O_3]$ from December to March
θ	-1.1 to -1.6	$64°$ to $42°$	-33%	36% to 53%
T	0.25 to 0.65	263 to 279 K	16%	4% to 10%
AH	0.02 to 0.04	2.7 to 4.2 mbar	56%	1% to 2%

335

Near the solstice, the solar zenith angle is insensitive to the date, so to calculate S_0, we modulated the latitude instead. The large value of S_0 helps explain the rarity of the winter ozone phenomenon. Apparently, it is only expected in a narrow range of latitudes. The Uinta and Upper Green River Basins are respectively at about the 40th and 42nd parallels. At just the 45th parallel, with a 12% increase in noon-time solar zenith angle relative to the Uinta Basin, we can expect ozone concentrations to decrease by about 13%
340 to 19%. Therefore, we expect the oil and gas fields of Alberta and Alaska to be spared from winter ozone. Since snow cover is also required for winter ozone, we also expect it to be rare at lower latitudes (Mansfield and Hall; 2018). If global warming causes the snow line to drift farther north, high winter ozone concentrations may become rare even at the 40th to the 42nd parallel.

345

6 Discussion and conclusions

The trend in photochemical indicators documented in Figs. 2 and 3 is dominated more by an increase in NO_x sensitivity than a decrease in VOC sensitivity. S_{NO_x} increases from values below S_{VOC} and near zero while S_{VOC} remains relatively flat. In the early
350 season, S_{NO_x} is often negative.

Figure 11 demonstrates that two separate effects are responsible for the trend in photochemical indicators documented in Figs. 2 and 3:

355 First, meteorological drivers dominated by the solar zenith angle push the indicator curves to higher levels as the season progresses, increasing and decreasing, respectively, the extents of the NO_x-sensitive and NO_x-saturation domains. Temperature and absolute humidity also drive the indicator curves upward, but their impact is smaller.

Second, the downward trend in NO_x concentration documented in Fig. 5 pushes typical concentration ranges, the white rectangles

360 in Fig. 11, downward. In late December, the rectangle lies predominantly in the NO_x-saturation domain while in early March it lies in the NO_x-sensitivity domain. This downward trend in NO_x concentration is probably the result of both dilution and emission effects. Dilution occurs because the typical mixing height increases with the passing season. Emissions change because there are processes and equipment linked to the temperature. Methane concentrations (and presumably by extension, non-methane VOC concentrations) also decrease with the advancing season.

365

The results in Fig. 11 indicate that, all else being equal, ozone concentrations intensify as the season progresses. The calculation in Table 5 indicates that the solar zenith angle is the most important variable driving this increase.

On the basis of these results, we recommend that Uinta Basin ozone mitigation be focused on controlling both NO_x and VOC. NO_x

370 controls in early winter could conceivably stimulate higher ozone (whenever $S_{NO_x} < 0$), but there are fewer daily exceedances then (Fig. 12) with lower ozone on average (Fig. 11), and any early-winter ozone increases will probably be more than offset by decreases in February and March.
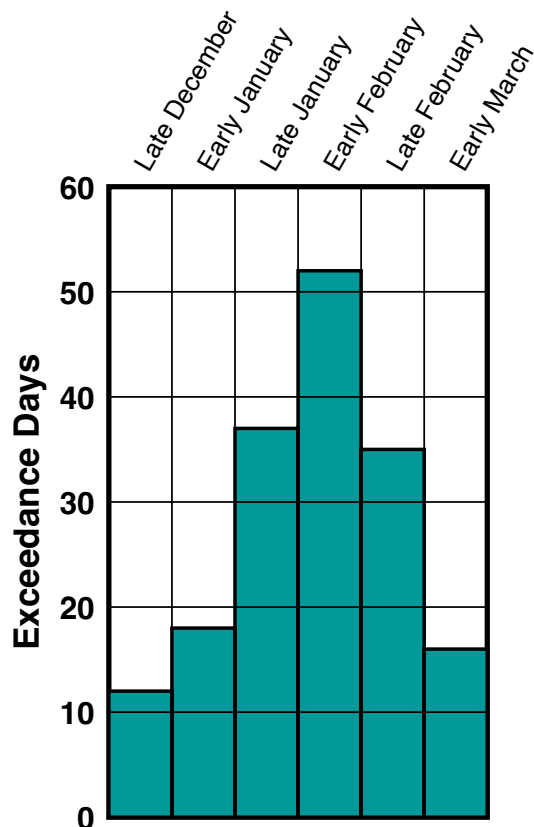
375 **Figure 12. The number of days in each of the six fortnights between December 2009 and March 2020 during which the 8-hour average ozone concentration at the Ouray monitoring station (central Uinta Basin) exceeded 70 ppb.**

As already mentioned, seasonal trends in the photochemical regime are very common throughout the Northern Hemisphere (Kleinman, 1991; Jacob et al., 1995; Liang et al., 1998; Martin et al., 2004; Jin et al., 2017). This study identifies the primary

380 drivers for the trend in the Uinta Basin from late December to early March. No doubt these drivers have a similar effect elsewhere, but we should be cautious in extending these results to other regions. For example, biogenic emissions are probably a more important driver of seasonal trends in many regions than they are in the arid Uinta Basin. However, the fact that such trends are ubiquitous may derive from the fact that the actinic flux is the single most important driver in all regions.

385 Acknowledgements

Competing Interests

390 The authors have no competing interests.

Author Contributions

SNL compiled the observational data and developed the initial F0AM code. MLM ran the F0AM models, analysed their results, and composed the manuscript.

395

References

Ahmadov, R., McKeen, S., Trainer, M., Banta, R., Brewer, A., Brown, S., Edwards, P. M., de Gouw, J. A., Frost, G. J., Gilman, J., Helmig, D., Johnson, B., Karion, A., Koss, A., Langford, A., Lerner, B., Olson, J., Oltmans, S., Peischl, J., Pétron, G., Pichugina, Y., Roberts, J. M., Ryerson, T., Schnell, R., Senff, C., Sweeney, C., Thompson, C., Veres, P. R., Warneke, C., Wild, R., Williams,

400 E. J., Yuan, B., Zamora, R.: Understanding high wintertime ozone pollution events in an oil- and natural gas-producing region of the western US, Atmos. Chem. Phys., 15, 411-429, doi: 10.5194/acp-15-411-2015, 2015.

Bishop, G. A., Haugen, M. J., McDonald, B. C., Boies, A. M.: Utah Wintertime Measurements of Heavy-Duty Vehicle Nitrogen Oxide Emission Factors, Env. Sci. Tech., 56, 1885-1893, 2022, 56, 3, 1885–1893, doi: 10.1021/acs.est.1c06428, 2022.

Choi, Y., Kim, H., Tong, D., Lee, P.: Summertime weekly cycles of observed and modeled NO_x and O_3 concentrations as a function

405 of satellite derived ozone production sensitivity and land use types over the Continental United States, Atmos. Chem. Phys., 12, 6291-6307, doi: 10.5194/acp-12-6291-2012, 2012.

Chou, C. C-K., Tsai, C.-Y., Shiu, C.-J., Liu, S. C., Zhu, T.: Measurement of NO_y during Campaign of Air Quality Research in Beijing 2006 (CAREBeijing-2006): Implications for the ozone production efficiency of NO_x, J. Geophys. Res., 114, D00G01, doi: 10.1029/2008JD010446, 2009.

410   Dardiotis, C., Martini, G., Marotta, A., Manfredi, U.: Low-temperature cold-start gaseous emissions of late technology passenger cars, Applied Energy, 111, 468-478, doi: 10.1016/j.openergy.2013.04.093, 2013.

Duncan, B. N., Yoshida, Y., Olson, J. R., Sillman, S., Martin, R. V., Lamsal, L., Hu, Y., Pickering, K. E., Retscher, C., Allen, D. J., Crawford, J. H.: Application of OMI observations to a space-based indicator of NOₓ and VOC controls on surface ozone formation, Atmos. Env., 44, 2213-2223, doi: 10.1016/j.atmosevn.2010.03.010, 2010.

415   Edwards, P. M., Brown, S. S., Roberts, J. M., Ahmadov, R., Banta, R. M., deGouw, J. A., Dubé, W. P., Field, R. A., Flynn, J. H., Gilman, J. B., Graus, M., Helmig, D., Koss, A., Langford, A. O., Lefer, B. L., Lerner, B. M., Li, R., Li, S.-M., McKeen, S. A., Murphy, S. M., Parish, D. D., Senff, C. J., Soltis, J., Stutz, J., Sweeney, C., Thompson, C. R., Trainer, M. K., Tsai, C., Veres, P. R., Washenfelder, R. A., Warneke, C., Wild, R. J., Young, C. J., Yuan, B., Zamora, R.: High winter ozone pollution from carbonyl photolysis in an oil and gas basin, Nature, 514, 351-354, doi: 10.1038/nature13767, 2014.

420   Finlayson-Pitts, B. J., Pitts, Jr., J. N.: *Chemistry of the Upper and Lower Atmosphere,* Academic Press, San Diego, 2000.

Grange, S. K., Farren, N. J., Vaughan, A. R., Rose, R. A., Carslaw, D. C.: Strong Temperature Dependence for Light-Duty Diesel Vehicle NOₓ Emissions, Env. Sci. Tech., 53, 6587-6596, doi: 10.1021/acs.est.9b01024, 2019.

425   Hall, D. L., Anderson, D. C., Martin, C. R., Ren, X., Salawitch, R. J., He, H., Canty, T. P., Hains, J. C., Dickerson, R. R.: Using near-road observations of CO, NOᵧ, and CO₂ to investigate emissions from vehicles: Evidence for an impact of ambient temperature and specific humidity, Atmos. Env., 232, 117558, doi: 10.1016/j.atmosenv.2020.117558, 2020.

Jacob, D. J., Horowitz, L. W., Munger, J. W., Heikes, B. G., Dickerson, R. R., Artz, R. S., Keene, W. C.: Seasonal transition from NOₓ- to hydrocarbon-limited conditions for ozone production over the eastern United States in September, J. Geophys. Res., 100
430   (D5), 9315-9324, doi: 10.1029/94JD03125, 1995.

Jenkin, M. E., Saunders, S. M., Wagner, V., Pilling, M. J.: Protocol for the development of the Master Chemical Mechanism, MCM v3 (Part B): tropospheric degradation of aromatic volatile organic compounds, Atmos. Chem. Phys., 3, 181-193, doi: 10.5194/acp-3-181-2003, 2003.

Jenkin, M. E., Young, J. C., Rickard, A. R.: The MCM v3.3.1 degradation scheme for isoprene, Atmos. Chem. Phys., 15, 11433-
435   11459, doi: 10.5194/acp-15-11433-2015, 2015.

Jin, X., Fiore, A. M., Murray, L. T., Valin, L. C., Lamsal, L. N., Duncan, B., Boersma, K. F., De Smedt, I., Gonzalez Abad, G., Chance, K., Tonnesen, G. S.: Evaluating a Space-Based Indicator of Surface Ozone-NOₓ-VOC Sensitivity Over Midlatitude Source Regions and Application to Decadal Trends, J. Geophys. Res: Atmos., 122, 10,439-10,491, doi: 10.1002/2017JD026720, 2017.

Kendall, M. G.: *Rank Correlation Methods*, 4th ed., London, Griffin, 1975.

440   Kerry, K. E., and Hawick, K. A.: Kriging interpolation on high-performance computers, in Sloot, P., Bubak, M., Hertzberger, B. (eds.), High Performance Computing and Networking, HPCN-Europe 1998, Lecture Notes in Computer Science, 1401, Spring, Berlin, doi: 10.1007/BFb0037170, 1998.

Kleinman, L. I.: Seasonal Dependence of Boundary Layer Peroxide Concentration: The Low and High NOₓ Regimes, J. Geophys. Res., 96, (D11), 20,721-20,733: doi: 10.1029/91JD02040, 1991.

445   Largeron, Y., Staquet, C.: Persistent inversion dynamics and wintertime PM₁₀ air pollution in Alpine valleys, Atmos. Env., 135, 92-108, doi: 10.1016/j.atmosenv.2016.03.045, 2016.

Li, K., Jacob, D. J., Liao, H., Qiu, Y., Shen, L., Zhai, S., Bates, K. H., Sulprizio, M. P., Song, S., Lu, X., Zhang, Q., Zheng, B., Zhang, Y., Zhang, J., Lee, H. C., Kuk, S. K.: Ozone pollution in the North China Plain spreading into the late-winter haze season, Proc. Nat. Acad. Sci., 118, 10, e2015797118, doi: 10.1073/pnas.2015797118, 2021.

450   Li, X., Dallmann, T. R., May, A. A., Presto, A. A.: Seasonal and Long-Term Trend of on-Road Gasoline and Diesel Vehicle Emission Factors Measured in Traffic Tunnels, Appl. Sci., 10, 2458, doi: 10.3390/app10072458, 2020.

Liang, J., Horowitz, L. W., Jacob, D. J., Wang, Y., Fiore, A. M., Logan, J. A., Gardner, G. M., Munger, J. W.: Seasonal budgets of reactive nitrogen species and ozone over the United States, and export fluxes to the global atmosphere, J. Geophys. Res., 103: D11, 13,435-13,450, doi: 10.1029/92JD03126, 1998.

455   Lyman, S., Mansfield, M., Shorthill, H.: Final Report: 2013 Uintah Basin Winter Ozone & Air Quality Study, pp. 23-31, https://www.usu.edu/binghamresearch/files/2013-final-report-uimssd-R.pdf

Lyman, S., Mansfield, M., Tran, H., Tran, T.: 2018 Annual Report: Uinta Basin Air Quality Research," pp. 33-35, https://www.usu.edu/binghamresearch/files/reports/UBAQR-2018-AnnualReport.pdf

Lyman, S. N., Holmes, M., Tran, H., Tran, T., O'Neil, T.: High ethylene and propylene in an area dominated by oil production,
460   Atmosphere, 12, 1, doi: 10.3390/atmos12010001, 2021.

Mansfield, M. L., Hall, C. F.: Statistical analysis of winter ozone events, Air Qual. Atmos. Health, 6, 687-699, doi: 10.1007/s11869-013-0204-0, 2013.

Mansfield, M. L., Hall, C. F.: A survey of valleys and basins of the western United States for the capacity to produce winter ozone, J. Air Waste Manag. Assoc., 68, 909-919, doi: 10.1080/10962247.2018.1454356, 2018.

465   Mann, H. B.: Nonparametric tests against trend, Econometrica, 13, 245-259, doi: 10.2307/1907187, 1945.

Martin, R. V., Fiore, A. M., Van Donkelaar, A.: Space-based diagnosis of surface ozone sensitivity to anthropogenic emissions, Geophys. Res. Lett., 31, L06120, doi: 10.1029/2004GL019416, 2004.

MCM 2022: The Master Chemical Mechanism, http://mcm.york.ac.uk/, last referenced 02/2022.

Matichuk, R., Tonnesen, G., Luecken, D., Gilliam, R., Napelenok, S. L., Baker, K. R., Schwede, D., Murphy, B., Helmig, D.,
470   Lyman, S., Roselle, S.: Evaluation of the Community Multiscale Air Quality Model for Simulating Winter Ozone Formation in the Uinta Basin, J. Geophys. Res. Atmos., 122, 13545-13572, doi: 10.1002/2017JD027057, 2017.

NASA Giovanni 2022: https://giovanni.gsfc.nasa.gov/giovanni/, last referenced 09/2024.

NASA OMI 2022: https://www.earthdata.nasa.gov/learn/find-data/near-real-time/omi, last referenced 09/2022.

NOAA GML 2022: https://gml.noaa.gov/ccgg/trends_ch4/, last referenced 09/2022.

475   Reiter, M. S., Kockelman, K. M.: The problem of cold starts: A closer look at mobile source emission levels, Transp. Res. Part D, 43, 123-132, doi: 10.1016/j.trd.2015.12.012, 2016.

Rickard, A. R., Salisbury, G., Monks, P. S., Lewis, A. C., Baugitte, S., Bandy, B. J., Clemitshaw, K. C., Penkett, S. A.: Comparison of Measured Ozone Production Efficiencies in the Marine Boundary Layer at Two European Coastal Sites under Different Pollution Regimes, J. Atmos. Chem., 43, 107-134, doi: 10.1023/A:1019970123228, 2002.

480   Saha, P. K., Khlystov, A., Snyder, M. G., Grieshop, A. P.: Characterization of air pollutant concentrations, fleet emission factors, and dispersion near a North Carolina interstate freeway across two seasons, Atmos. Env., 177, 143-153, doi: 10.1016/j.atmosenv.2018.01.019, 2018.

Saunders, S. M., Jenkin, M. E., Derwent, R. G., Pilling, M. J.: Protocol for the development of the Master Chemical Mechanism, MCM v3 (Part A): tropospheric degradation of non-aromatic volatile organic compounds, Atmos. Chem. Phys., 3, 161-180, doi:
485   10.5194/acp-3-161-2003, 2003.

Schnell, R. C., Oltmans, S. J., Neely, R. R., Endres, M. S., Molenar, J. V., White, A. B.: Rapid photochemical production of ozone at high concentrations in a rural site during winter, Nature Geoscience, 2, 120, doi: 10.1038/ngeo415, 2009.

Seinfeld, J. H., Pandis, S. N.: *Atmospheric Chemistry and Physics: From Air Pollution to Climate Change,* 2nd ed., Wiley (2006). See pp 215 ff for a discussion of ozone production efficiency; p 765 for the formula to calculate the saturation vapor pressure of

490   water.

Shah, V., Jacob, D. J., Li, K., Silvern, R F., Zhai, S., Liu, M., Lin, J., Zhang, Q.: Effect of changing NO_x lifetime on the seasonality and long-term trends of satellite-observed tropospheric NO_2 columns over China, Atmos. Chem. Phys., 20, 1483-1495, doi: 10.5194/acp-20-1483-2020, 2020.

Sillman, S.: The use of NO_y, H_2O_2, and HNO_3 as indicators for ozone-NO_x-hydrocarbon sensitivity in urban locations, J. Geophys.

495   Res., 100 (D7), 14,175-14,188, doi: 10.1029/94JD02953, 1995.

Sillman, S., He, D., Cardelino, C., Imhoff, R. E.: The Use of Photochemical Indicators to Evaluate Ozone-NOx-Hydrocarbon Sensitivity: Case Studies from Atlanta, New York, and Los Angeles, Journal of the Air & Waste Management Association, 47:10, 1030-1040, doi: 10.1080/10962247.1997.11877500, 1997.

Sillman, S., He, D., Pippin, M. R., Daum, P. H., Imre, D. G., Kleinman, L. I., Lee, J. H., Weinstein-Lloyd, J.: Model correlations

500   for ozone, reactive nitrogen, and peroxides for Nashville in comparison with measurements: Implications for O_3-NO_x-hydrocarbon chemistry, J. Geophys. Res., 103 (D17), 22,629-22,644, doi: 10.1029/98JD00347, (1998).

Sillman, S.: The relation between ozone, NO_x and hydrocarbons in urban and polluted rural environments, Atmos. Env., 33, 1821-1845, doi: 10.1016/S1352-2310(98)00345-8, 1999.

Sillman, S., He, D.: Some theoretical results concerning O_3-NO_x-VOC chemistry and NO_x-VOC indicators, J. Geophys. Res., 107

505   (D22), 4659, doi: 10.1029/2001JD001123, 2002.

Suarez-Bertoa, R., Astorga, C.: Impact of cold temperature on Euro 6 passenger car emissions, Environmental Pollution, 234, 318-329, doi: 10.1016/j.envpol.2017.10.096, 2018.

Wærsted, E. G., Sundvor, I., Denby, B. R., Mu, Q.: Quantification of temperature dependence of NO_x emissions from road traffic in Norway using air quality modeling and monitoring data, Atmospheric Environment: X, 13, 100160, doi:

510   10.1016/j.aeaoa.2022.100160, 2022.

Wang, L., Wang, J., Tan, X., Fang, C.: Analysis of NO_x Pollution Characteristics in the Atmospheric Environment in Changchun City, Atmosphere, 11, 30, doi: 10.3390/atmos11010030, 2020.

Weber, C., Sundvor, I., Figenbaum, E.: Comparison of regulated emission factors of Euro 6 LDV in Nordic temperatures and cold start conditions: Diesel- and gasoline direct-injection, Atmospheric Environment, 206, 208-217, doi:

515   10.1016/j.atmosenv.2019.02.031, 2019.

Whiteman, C. D., Eisenbach, S., Pospichal, B., R. Steinacker, R.: Comparison of Vertical Soundings and Sidewall Air Temperature Measurements in a Small Alpine Basin, Journal of Applied Meteorology and Climatology, 43, 1635-1647, doi: 10.1175/JAM2168.1, 2004.

Wolfe, G. M., Marvin, M. M., Roberts, S. J., Travis, K. R., J. Liao, J.: The Framework for 0-D Atmospheric Modeling (F0AM)

520   v3.1, Geoscientific Model Development, doi: 10.5194/gmd-2016-175, 2016.

Zong, R., Xue, L., Wang, T., Wang, W.: Inter-comparison of the Regional Atmospheric Chemistry Mechanism (RACM2) and Master Chemical Mechanism (MCM) on the simulation of acetaldehyde, Atmospheric Environment, 186, 144-149, doi: 10.1016/j.atmosenv.2018.05.013, 2018.